frontiers in Materials

ORIGINAL RESEARCH
published: 10 November 2020
doi: 10.3389/fmats.2020.588399

Softwood Kraft Pulp-Derived Carbon-Supported PtNi Catalysts for the Electrooxidation of Ethanol

María Luz Nieva Lobos[1], *Juan Manuel Sieben*[2]* *and Elizabeth Laura Moyano*[1]

[1]INFIQC, Departamento de Química Organica, Facultad de Ciencias Químicas, Universidad Nacional de Córdoba, Córdoba, Argentina, [2]Instituto de Ingeniería Electroquímica y Corrosión (INIEC) and CONICET, Departamento de Ingeniería Química, Universidad Nacional del Sur, Bahía Blanca, Argentina

In this work, the biocarbons synthesized by fast pyrolysis at 350°C of raw (BK) and H_3PO_4 treated (TBK) fibrous fraction of non-bleached softwood kraft pulp has been proposed as novel supports for the deposition of PtNi nanocatalysts. The bimetallic nanoparticles were deposited by pulse microwave-assisted reduction using ethylene glycol both as solvent and reducing agent. The physicochemical properties of the resulting materials were evaluated by means of X-ray diffraction, transmission electron microscopy, energy dispersive X-ray microanalysis, and inductively coupled plasma atomic emission spectroscopy, whereas the electrochemical activity towards ethanol oxidation in acid medium was evaluated using cyclic voltammetry and chronoamperometry. Nanosized PtNi particles with average diameters in the range of 2.9–4.1 nm and a nickel content of ca. 30 at% were deposited over both softwood kraft pulp-derived carbon materials. The electrochemical measurements showed that the bimetallic nanoparticles deposited over the acid-treated biocarbon (PtNi/TBK) exhibit superior catalytic performance in terms of activity, onset potential, and poisoning tolerance. The mass activity of the PtNi nanocatalyst supported over TBK was about 1.3 and 6.3 times higher than that of the bimetallic nanoparticles deposited onto BK and Pt/C, respectively. The effect of the carbonaceous material on the electrocatalytic activity is discussed in detail.

Keywords: biocarbons, fast pyrolysis, PtNi nanoparticles, microwave-assisted synthesis, ethanol oxidation

OPEN ACCESS

Edited by:
Jong-Seok Oh,
Kongju National University,
South Korea

Reviewed by:
Biuck Habibi,
Azarbaijan Shahid Madani University,
Iran
Yawen Tang,
Nanjing Normal University, China

***Correspondence:**
Juan Manuel Sieben
jmsieben@uns.edu.ar

Specialty section:
This article was submitted to Energy Materials, a section of the journal Frontiers in Materials

Received: *28 July 2020*
Accepted: *15 October 2020*
Published: *10 November 2020*

Citation:
Nieva Lobos ML, Sieben JM and Moyano EL (2020) Softwood Kraft Pulp-Derived Carbon-Supported PtNi Catalysts for the Electrooxidation of Ethanol. Front. Mater. 7:588399. doi: 10.3389/fmats.2020.588399

INTRODUCTION

During the last years, the biocarbons have been proposed as the cheapest and eco-friendly alternative to replacing the commercial carbon black powders and other expensive materials such as carbon nanotubes and graphene in the electrodes of different electrochemical devices like fuel cells, supercapacitors, and batteries (Guo et al., 2014; da Silva et al., 2014; Nieva Lobos et al., 2016b; Liu et al., 2019; Pistone and Espro, 2020). Different biomass feedstock sources such as forestry and agro-industrial residues, as well as industrial and domiciliary wastes, can be employed for producing biocarbons by pyrolysis or hydrothermal methods. Accordingly, it is possible to effectively reduce energy consumption and fabrication costs and limit the emission of greenhouse gases. For instance, spruce and corncob hydrolysis by-products formed during bioethanol synthesis were employed to producing activated biocarbons via hydrothermal carbonization and subsequent chemical activation using KOH (Falco et al., 2013). A N-doped biocarbon material was fabricated by the pyrolysis of chitosan at 900°C under N_2 atmosphere and then utilized as support of Pt nanoparticles for methanol

electrooxidation (Zhao et al., 2014). On the other hand, a low-cost biosynthesis method using yeast cells as the precursor was used to fabricate a nitrogen- and phosphorus-doped biocarbon, which was employed as an electrode material for the oxygen reduction reaction (ORR) (Gong et al., 2015). More recently, coconut shells were used for the synthesis of biocarbons by hydrothermal carbonization and then subjected to physical, chemical, or thermal activation (Schonvogel et al., 2019). The coconut shell-derived carbon powders were used as supports of platinum nanoparticles for the ORR process.

Apart from those mentioned above, the pulp and paper mills produce huge amounts of residual biomass, which are usually disposed of in waste dumps or incinerated, thus causing serious damage to the environment (Reckamp et al., 2014). Moreover, the high concentration of lignocellulosic compounds in the wastewater produces eutrophication of water bodies, which endangers aquatic life (Haq and Raj, 2020). The treatment of these residues via fast pyrolysis can be a cost-effective and sustainable way to reduce contamination and to obtain valuable products such as biofuels and biocarbons. Reckamp et al. produced biochar and bio-oils via the fast pyrolysis of paper mill sludge subjected to acid hydrolysis and torrefaction pretreatments (Reckamp et al., 2014). Bengtsson and collaborators converted dry-jet wet spun fibers from a 70/30 w/w mixture of softwood kraft lignin and bleached softwood kraft pulp into carbon fibers by carbonization at various temperatures and different residence times (Bengstsson et al., 2020). Nieva Lobos et al. demonstrated that the fibrous fraction of unbleached softwood kraft pulp is an interesting material for the production of biocarbons via fast pyrolysis, since the content of lignin is very low (Nieva Lobos et al., 2016a). Herein, the kraft pulp residues can be transformed into valuable biocarbons through fast pyrolysis and the textural and surface properties can be tuned to provide a high accessible surface area and efficient anchoring sites to platinum-based catalysts for direct ethanol fuel cells (DEFCs).

Regarding platinum-based electrocatalysts, the bimetallic PtNi alloy system emerges as a promising alternative for the electrooxidation of ethanol in acidic electrolyte solutions because of the high resistance to dissolution of nickel atoms in the bimetallic alloy and the passivating role of Ni hydroxides at the direct ethanol fuel cell operating conditions (Antolini, 2017). Besides, nickel is a low-cost Earth-abundant transition metal. The beneficial effect of nickel on bimetallic PtNi catalysts for the electrooxidation of alcohols is associated either with its ability to form-OH labile species through the dissociation of water at a lower potential that on Pt, and the electronic and strain effects provoked by the cocatalyst in the platinum surface atoms (Antolini et al., 2005; Nørskov et al., 2009; Comignani et al., 2015; Altarawneh et al., 2018). Shen et al. studied the influence of Ni and Ru on the activity of PtNi and PtNiRu catalysts supported on graphene nanosheets for ethanol oxidation and discovered that Ni is responsible for reducing the bond strength and coverage of adsorbed poisoning species on Pt surface via strain and electronic effects (Shen et al., 2015). Beyhan and collaborators evaluated the performance of PtNi/C and PNiSn/C catalysts towards ethanol oxidation and revealed that nickel promotes the cleavage of the C-C bond (Beyhan, et al., 2013). Whereas Comignani et al. found that nickel oxide species facilitate the cleavage of the C-H and O-H bonds of ethanol both through the bifunctional mechanism and the ligand effect (Comignani et al., 2015). Habibi and coworkers studied the effect of Ni on PtNi nanoparticles supported on carbon-ceramic (Habibi and Dadashpour, 2013) and CuNiPt nanoparticles supported on graphitized pencil lead (Imanzadeh and Habibi, 2020) and suggested that the enhanced performance of the catalysts for the electrooxidation of ethanol is explained in terms of the bifunctional mechanism, the electronic effects and the augment in electroactive surface area due to the '"leaching out"' effect of the alloying element.

This work explores the possibility of using the biocarbons fabricated by fast pyrolysis of untreated and acid-treated fibrous fraction of kraft pulp waste as supports for the deposition of bimetallic PtNi nanoparticles. The as-synthesized biocarbons exhibited specific surface areas ranging from 306 to 454 $m^2\ g^{-1}$ and different oxygen and nitrogen contents. The bimetallic PtNi nanoparticles were deposited over the biocarbons derived from kraft pulp by pulse microwave-assisted reduction in ethylene glycol. Spherical PtNi particles of ca. 3.5 nm with a nickel content of about 30 at% were deposited over the surface of the biocarbons. The electrocatalytic performance of the as-prepared catalysts towards ethanol oxidation in acid medium was investigated by cyclic voltammetry and chronoamperometry. It was found that the bimetallic nanoparticles deposited on the surface of the biocarbon derived from acid-treated kraft pulp present a superior catalytic performance in terms of activity, onset potential and poisoning tolerance compared to the catalyst prepared with the untreated biocarbon, reaching peak current densities of 476 and 3,574 A g_{Pt}^{-1} at 25 and 60°C, respectively. The superior performance of the bimetallic nanoparticles supported over the acid-treated biocarbon was explained in terms of the carbon support effect on the properties of PtNi catalyst.

EXPERIMENTAL

Raw Material

Softwood kraft pulp (KP) was selected for the pyrolysis study. In the study, KP samples were chemical treated using a phosphoric acid solution (Anedra, 85% w/w). Typically, in the experiments 1.00 g of KP and 5 ml of 0.17 M H_3PO_4 aqueous solution were added in a round-bottom flask under magnetic stirring and kept at 80°C for 2 h. Afterward, the slurry was filtered under vacuum and the solid was dried for 8 h under reduced pressure at 40°C. The acid-treated material is named as A-KP from now on.

Characterization of Raw Materials

The samples KP and A-KP were characterized by elemental analysis with an Elemental Analyzer 2400 Serie II Perkin Elmer. The oxygen content was determined by difference, taking into account the ash content in the calculus. Ash content of kraft pulp materials was established by dry combustion at 575°C for 24 h. The raw and acid-treated kraft

pulp materials were also studied by X-ray diffraction (XRD). The X-ray patterns were acquired in a Philips PW1710 BASED instrument operating at 45 keV and 30 mA, using Cu-Kα radiation. Fourier Transform Infrared (FTIR) spectroscopy was carried out to analyze the surface chemistry of the samples. The spectra were obtained using a FTIR Bruker IFS 28v spectrometer, with a resolution of 2 cm^{-1} in the range of 4,000–400 cm^{-1} by using anhydrous KBr disks. Besides, pulp materials were studied by scanning electron microscopy (SEM) with a field emission scanning electron microscope FE-SEM, Sigma Zeiss apparatus. The content of cellulose, hemicellulose, and lignin in the starting biomass was determined using an ANKOM 200 fiber analyzer (ANKOM Technologies, USA), following a modified technique described by Goering and Van Soest with modifications (Van Soest et al., 1991).

Preparation of Biocarbons from Kraft Pulp

Biocarbons were prepared by pyrolysis of KP and A-KP. Pyrolysis experiments were performed under oxygen-free conditions using a quartz tubular reactor, which was placed in a tubular furnace with an internal thermocouple. Approximately 5.00 g of sample were put in a ceramic boat and then introduced in the middle of the pyrolysis reactor once the reaction temperature of 350°C and the vacuum conditions were reached. Ultra-dry nitrogen was used as the carrier gas to enhance the transportation of products to the condensation region at cryogenic temperatures. The flow rate of the carrier gas was kept at 0.1 ml s^{-1}, residence times were less than 5 s and the experiments lasted 20 min to attain the complete conversion of the biomass sample. Carbonaceous materials were removed from the ceramic boat and weighed. Biocarbon sample from KP is called BK while carbon from A-KP is called TBK, respectively. Additionally, BK and TBK were extensively washed with distilled water to remove remaining impurities in order to leave the porous structures free.

Physicochemical Characterization of Biocarbons

The physicochemical properties of BK and TBK samples were studied by elemental analysis, XRD, FTIR, and SEM using the instrumentation detailed in *Characterization of Raw Materials* for kraft pulp. Brunauer-Emmett-Teller (BET) surface area, total micropore volume and mesopore volume of the biochars were measured at least in duplicate by nitrogen gas sorption at −196°C using a NOVA 1000e porosimeter (Quantachrome, Boynton Beach, FL, USA). Samples were vacuum degassed overnight at 160°C before analysis.

The electrical conductivity of carbon powders was determined via the four-point procedure. The biocarbon sample (100.0 mg) was placed into a Teflon tube and then compressed at a pressure of 150 kPa between two brass electrodes of 8 mm in diameter. Electrical conductivity was calculated according to the following equation: $\sigma = h/(R \times A)$; where R is the resistance calculated by using Ohm's law, h is the powder thickness, and A is the surface area of the cylinder (Marinho et al., 2012). To ensure reproducibility the experiments were carried out in triplicate.

Synthesis of Catalysts

The bimetallic PtNi nanosized particles supported on the biocarbons were prepared by a pulse microwave-assisted method in ethylene glycol. A suitable amount of nickel (II) chloride hexahydrate (11.6 mg, $NiCl_2{\cdot}6H_2O$) and 100.0 mg of BK or TBK biocarbons were dissolved into 50 ml of ethylene glycol (EG) in a beaker by sonication for 60 min. Afterward, an appropriate volume of a diluted H_2PtCl_6 aqueous solution (0.0386 M) was added into the beaker. The suspension was sonicated for 15 min and then the pH value adjusted to 10.0 by adding 0.5 M KOH-EG solution. The deposition of the bimetallic PtNi nanoparticles on the biocarbons was carried out by microwave heating in an oven (2450 MHz, 700 W) under a pulse mode condition of 30 s on/45 s off for five pulses. The resulting slurries were cooled down to room temperature and the solid collected by vacuum filtration. The catalysts were rinsed repeatedly with bidistilled water and ethanol and finally dried for 24 h at 70°C in an oven. The nominal Pt:Ni atomic ratio was 2.35:1, and the total metal loading of the catalysts was 20 wt% on carbon. For comparison purposes, Pt/BK, Pt/TBK and Pt/C catalysts (20 wt% Pt on carbon) were synthesized using the same synthesis route. In the case of Pt/C catalyst, Vulcan XC-72 carbon black (BET area of 230 $m^2\ g^{-1}$, micropore volume of 0.36 $cm^3\ g^{-1}$, and conductivity of 0.195 S cm^{-1}) was used as the catalyst support (Comignani et al., 2017). Catalyst inks (1 mg ml^{-1}) were prepared by dispersing 10.0 mg of catalyst in a solution consisting of 7.96 ml of tridistilled water, 2 ml of isopropyl alcohol and 40 μL of Nafion ionomer solution (5 wt% in a mixture of lower aliphatic alcohols and water) by sonication for 45 min.

Electrochemical Characterization of Catalysts

The electrochemical experiments were run with a Princeton Applied Research VersaSTAT 3 potentiostat/galvanostat at 25 and 60°C. Three-electrode glass cells were employed to carry out the electrochemical tests. A saturated calomel electrode (*SCE*, +0.241 vs. *NHE*) located in a Luggin capillary served as the reference electrode while a platinum wire served as the counter electrode. The working electrodes were obtained by pipetting 20 μL of catalyst ink onto a polished glassy carbon rod (0.07 cm^2) to yield a catalyst loading of about 57 μg cm^{-2}. The electrodes were dried in air at room temperature for 3 h before use. The electrochemical behavior of the as-prepared electrocatalysts was performed by cyclic voltammetry (CV) in the range of −0.25–0.8 V for fifty cycles at a sweep rate of 0.05 V s^{-1} in 0.5 M H_2SO_4 at 25 °C. Before starting the experiments, all solutions were deaerated with pure N_2 for 30 min to remove dissolved electroactive oxygen. The performance of the electrodes for the alcohol electrooxidation was evaluated in 1 M EtOH/0.5 M H_2SO_4 in a potential range of −0.2 to 0.9 V at a scan rate of 0.05 V s^{-1}. The upper potential limit was restricted to 0.9 V in order to prevent or limit catalyst degradation and carbon corrosion. Furthermore, potentiostatic experiments (i.e., chronoamperometry) were carried out at an applied

potential of 0.5 V for 4,500 s. The catalytic activity is expressed in terms of current density per mass of Pt. The composition of the bimetallic catalysts before and after the long-term potentiostatic experiments were determined by EDX microanalysis.

The electroactive surface area (*ESA*) of the as-prepared electrocatalysts was determined by CO stripping voltammetry tests. CO stripping curves were obtained after bubbling CO through an electrochemical glass cell filled with N_2-purged 0.5 M H_2SO_4 solution for 20 min by holding the working electrode potential at -0.091 V, followed by N_2 bubbling to remove the excess of CO. Then, the CO stripping voltammogram curves were obtained by cycling the working electrode in the range of −0.091 to 0.8 V at a scan rate of 0.02 V s^{-1}. The stripping charges were determined between −0.091 and 0.8 V after current background correction. The *ESA* values were estimated by considering a monolayer charge of 420 μC cm^{-2} and an adsorption ratio of one CO molecule to each surface Pt site.

Physicochemical Characterization of Catalysts

The structure of the as-synthesized catalysts was evaluated by X-ray diffraction (XRD) using a Rigaku Dmax III C diffractometer with CuKα radiation source operated. The peak profiles in the X-ray patterns were fitted with the pseudo-Voigt function, employing the non-linear least-squares refinement procedure based on a finite-difference Marquardt algorithm. Lattice parameters and crystallite size were determined by Rietveld analysis. High-resolution transmission electronic microscopy (HR-TEM) images were obtained on a JEOL microscope (model JEM-2100 plus) operated at 200 keV. The average particle sizes were measured by counting approximately 200 particles in different sectors of each sample using free-software ImageJ. Furthermore, the composition distribution was investigated by elemental mapping using a microanalyzer INCA X-ray (Oxford Systems). The bulk composition of the catalysts was determined by energy dispersive X-ray (EDX) microanalysis with an EDAX probe coupled to a scanning electron microscope (SEM, JEOL 100). The analysis was performed in five different regions of each sample. The platinum and nickel loadings of the different catalysts were determined by inductively coupled plasma atomic emission spectrometry (ICP-AES) with a Shimadzu 1000 model III equipment.

RESULTS AND DISCUSSION

Characterization of Raw Material

The characteristics of the samples KP and A-KP are summarized in **Table 1**. The major organic elements in raw materials KP and A-KP are carbon and oxygen. For these materials, the oxygen and carbon content was similar, the concentration of hydrogen and nitrogen was very small, while sulfur was detected in traces. The main component of kraft pulp is cellulose, although hemicellulose and lignin are also present in few amounts. **Supplementary Figure S1** shows the X-ray diffraction patterns of KP and A-KP. It can be identified three-wide crystalline peaks at Bragg angles of around 16, 22 and 35°, which can be ascribed to the crystalline structure of cellulose (Klemm et al., 2005). The figures show that there are differences in the width of these peaks. It is observed that the width of the peaks of the KP is narrower than those of A-KP. Consequently, the chemical pretreatment of KP reduced the number of ordered microregions of the cellulose component, producing an increase in the presence of amorphous regions. This phenomenon has been observed in previous studies concerning the chemical treatment of cellulosic and lignocellulosic biomasses (Dobele et al., 2001; Zhang et al., 2009).

TABLE 1 | Properties of kraft pulp.

	KP[a]	A-KP[b]
C (wt%)[c]	46	43
N (wt%)[c]	0.8	0.7
H (wt%)[c]	5	4
O (wt%)[d]	41	40
S (wt%)[c]	0.03	0.04
Ash (wt%)[c]	7	11
Cellulose (g/Kg)[c]	81	-
Hemicellulose (g/Kg)[c]	9	-
Lignin (g/Kg)[c]	5	-

[a]*Raw kraft pulp.*
[b]*Acid-treated kraft pulp.*
[c]*Dry basis.*
[d]*Calculated by difference.*

To analyze the morphological change of kraft pulp after acid treatment, SEM measurements were performed. **Supplementary Figure S2A** and SI2B show the morphological characteristics of the kraft pulp sample before and after acid impregnation with phosphoric acid. For the non-treated sample (**Supplementary Figure S2A**), cellulose ribbons are clearly observed together with small amorphous regions. On the contrary, the A-KP sample is comprised of a great number of cellulose agglomerates with a very irregular surface. After acid treatment, the fibers are distinctly reduced in length compared with KP (**Supplementary Figure S2A**). According to these findings, the acid treatment caused more structural defects in the surface, probably by acid-catalyzed dehydration reactions of the cellulose component (Zhao et al., 2007).

The FT-IR spectra of KP and A-KP were very similar (**Supplementary Figure S3**). Samples were characterized by a dominant O-H stretch band (ca. 3,300 cm^{-1}) and a C-H band (ca. 2,900 cm^{-1}) attributed to the presence of aliphatic groups. The band at 1,638 cm^{-1} is ascribed to the bending mode of absorbed water. The bands at 1,428 and 1,363–1,362 cm^{-1} reveal the C-H symmetric and asymmetric deformations, respectively. The absorbance band at 1,314–1,313 cm^{-1} and 1,334 cm^{-1} are associated with the C-C and C-O skeletal vibrations. The region of 1,200–1,000 cm^{-1} is dominated by ring vibrations overlapped with stretching vibrations of (υ C-OH) side groups and the (υ C-O-C) glycosidic bond vibration. These bands are significant in both spectra, particularly the band at

TABLE 2 | Properties of biocarbons from kraft pulps.

Samples	Ultimate analysis (wt%)[a]				S_{BET}[c] (m^2 g^{-1})	Pore volume (cm^3 g^{-1})	σ[d] (S cm^{-1})
	C	H	N	O[b]			
BK[e]	71	2	1	21	306	1.2	0.029
TBK[f]	65	5	2	24	454	1.8	0.027

[a]*Dry basis.*
[b]*Calculated by difference.*
[c]*BET (Brunauer–Emmett–Teller) surface area.*
[d]*Electrical conductivity determined at a pressure of 150 kPa.*
[e]*Raw kraft pulp.*
[f]*Acid-treated kraft pulp.*

1,055–1,054 cm^{-1} is dominated by glycosidic bond (υ C-O-C) contribution. A small sharp band at 897–895 cm^{-1} is characteristic of β-glycosidic bonds between the sugar units in cellulose (Kacuráková et al., 2000).

Biocarbons Characterization

Table 2 shows the elemental analysis and superficial area for the biocarbons produced from fast pyrolysis of kraft pulp (BK) and acid-treated kraft pulp (TBK). These carbonaceous materials were obtained at 350°C. Comparing KP and A-KP with the carbons formed from these materials BK and TBK, respectively, it can be observed that the content of carbon increased after pyrolysis while the content of oxygen decreased (Tzong-Horng, 2010; González-García et al., 2013). This result would indicate that the raw material was richer in oxygen groups that could be eliminated after the thermal process due to the dehydration and carbonization reactions of the structural cellulose polymers. The specific surface area of the biocarbon obtained by the pyrolysis of KP is fairly good and this increased considerably with the acid treatment of the raw material. The increase in BET surface area can be ascribed to the liberation of certain volatile compounds as a result of the phosphoric acid activation treatment on the precursor material containing organic and inorganic materials. The surface area obtained mainly comes from the vaporization of organic matter during the pyrolysis process and chemical activation, leaving the porous surface. These results were consistent with previous studies concerning the production of biochar research (Kennedy et al., 2004; Tzong-Horng, 2010). In addition, the electrical conductivity values of both biocarbons were very close, indicating a similar degree of graphitization.

Figure 1 shows the morphology of BK and TBK carbons. The surface morphology was studied to know how affect the acid treatment to the raw material after pyrolysis. BK exhibited an irregular and roughness surface without any observable pore (**Figures 1A,B**). From the figure, it can be established that the shape of the cellulose macrofibrils was preserved after the pyrolysis process. **Figure 1C** shows the biocarbon obtained by the fast pyrolysis of acid-treated pulp. This material presented a rough surface showing irregular open and interconnected pores, which are of different sizes in the nanoscale range. This change in the morphology of the carbons can be associated with the chemical activation of starting material before the pyrolysis step which helped in the increase in porosity of the final material (El Qada et al., 2008; Sun et al., 2018). These pores are very useful for improving the specific surface area of biocarbons as was also seen in the obtained BET surface areas. **Supplementary Figure S4** shows the diffraction patterns of BK and TBK materials. In the case of BK, it can be seen the presence of

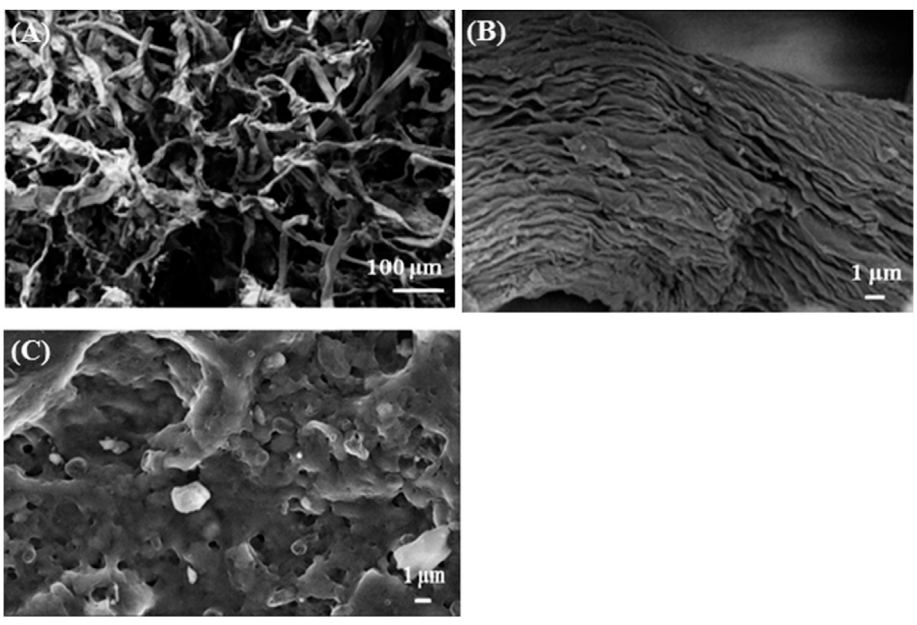

FIGURE 1 | Scanning electron microscope (SEM) images of: **(A)** BK at low magnification, **(B)** BK at higher magnification, and **(C)** TBK.

smaller signs that are due to calcite ($CaCO_3$) and quartz (SiO_2) between 25 and 35° that disappear when KP was treated with phosphoric acid.

FT-IR spectra corresponding to carbons from KP and A-KP are presented in **Figure 2**. The profile of both spectra is very similar in frequency absorption and intensity. The broad O-H band due to the stretching vibration mode of hydroxyl functional moieties is analogous to what is observed in the initial pulp samples. Contrary to what was obtained in the raw material, the bands associated with aliphatic/aromatic asymmetric C-H and symmetric C-H stretching can be seen as a broad and very weak peak at 2,990–2,820 cm^{-1}. In BK as well as TBK, carbonyl and olefinic groups can be easily detected. For instance, the absorption band at 1,706–1,700 cm^{-1} is assigned to C=O stretching vibrations that indicate the existence of ketones or aldehydes. The strong bands appearing in the 1,650–1,580 cm^{-1} region can be associated with C=C vibrations from aromatic rings. It is also evident for the appearance of these new peaks that the dehydration of the cellulose, the main constituent of pulps, has occurred. Also, for the same reason, the absorption patterns at 1,450–1,300 and 1,160–900 cm^{-1} were largely minimized for pulps during pyrolysis.

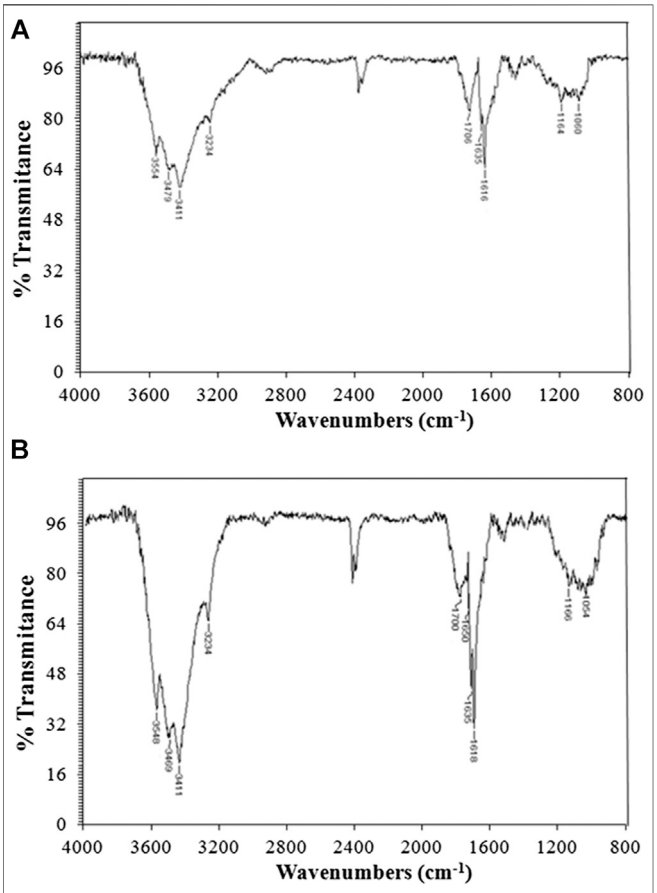

FIGURE 2 | FT-IR spectra of: **(A)** biocarbon from raw kraft pulp (BK) and **(B)** biocarbon from acid-treated kraft pulp (TBK).

Physicochemical Characterization of the As-Prepared Electrocatalysts

An EDX spectrum of the bimetallic PtNi nanoparticles supported on TBK biocarbon is displayed in **Figure 3A** and the results for the as-prepared electrocatalysts are summarized in **Table 3**. The spectrum exhibits the characteristic M and L X-ray lines of platinum and the K peaks of Ni. The average compositions of the bimetallic catalysts were in close agreement with the nominal values. In addition, the atomic composition of the electrocatalysts was also established by ICP-AES analysis. It can be observed that the Pt:Ni atomic ratios are very similar to the overall bulk compositions determined by EDX analysis.

Figure 3B shows the X-ray diffraction patterns of the as-synthesized PtNi nanoparticles supported on BK and TBK biocarbons. The diffractogram of Pt/C catalyst is also included for the sake of comparison. All diffraction patterns show four peaks at 2θ angles of ca. 40, 47, 68 and 82°, which are attributed to the (111), (200), (220) and (311) crystallographic planes of fcc platinum lattice structures (JCPDS Card No. 04–0783). It can be observed that the bimetallic PtNi nanoparticles supported on the biocarbons exhibit principally a single-phase disordered structure. On the other hand, the diffraction peaks of PtNi/BK and PtNi/TBK catalysts were slightly shifted towards higher 2θ angles compared to the reflections of Pt/C catalyst. This observation can be associated with the lattice contraction produced by partial substitution of Pt atoms with smaller Ni atoms, suggesting the formation of an alloy between Pt and Ni. Therefore, the lattice parameter (a_{fcc}) and lattice spacing (d_{hkl}) of PtNi/BK and PtNi/TBK catalysts are smaller than those of Pt/C (**Table 3**). The interplanar spacing between adjacent planes with the Miller indices (111) for PtNi/BK and PtNi/TBK are 2.22 and 2.21 Å respectively, while the d-spacing in Pt/C catalyst is 2.25 Å.

The atomic fraction of Ni in the solid solution can be estimated from Vegard's law using the following equation:

$$\boldsymbol{a_{PtNi} = (1 - x)a_{Pt} + x\, a_{Ni}} \quad (1)$$

where x is the molar of Ni, a_{Pt} is the lattice constant of pure Pt (0.3923 nm, JCPDS Card No. 004–0783), a_{Ni} is the lattice constant of pure Ni (0.3524 nm, JCPDS Card No. 004–0850) and a_{PtNi} is the measured lattice constant of the alloy.

According to the calculations, the Ni content in the bimetallic alloy is 12 at% for the PtNi/BK catalyst and 19 at% for the PtNi/TBK catalyst. A comparison of the nickel contents determined from the EDX and ICP-AES analyses and the ratios calculated from the lattice parameters through the Vegard's law discloses that some fraction of the Ni atoms are forming a non-alloyed phase probably comprised of oxides and hydroxides. The absence of the diffraction peaks from NiOOH, $Ni(OH)_2$ and/or NiO species in the X-ray patterns of the bimetallic materials may be associated with the existence of an amorphous state. This is in accordance with previous results published in the literature (Zhou et al., 2011; Luo et al., 2013; Shen et al., 2015). It can be calculated that only about 37% of Ni atoms are forming an alloy with Pt in the PtNi/BK catalyst, while ca. 61% of Ni atoms are forming an

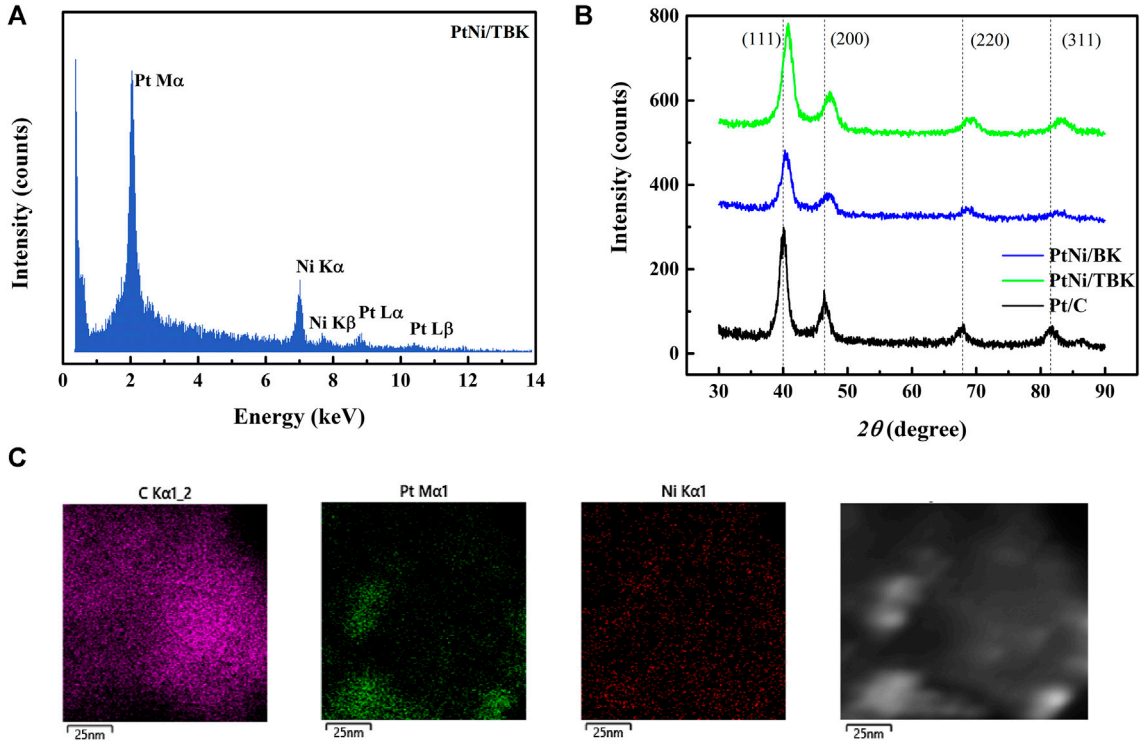

FIGURE 3 | (A) Representative EDX spectrum of PtNi/TBK catalyst. **(B)** X-ray diffraction patterns of the as-prepared electrocatalysts. **(C)** Representative EDX mapping image of PtNi/TBK catalyst and corresponding HAADF-STEM image.

alloy with the noble metal in the PtNi/TBK catalyst. **Figure 3C** displays a representative EDX mapping image of PtNi/TBK catalyst. The spherical nanoparticles exhibit a homogeneous distribution of Pt and Ni elements, revealing that both metals were reduced simultaneously onto the surface of the biocarbon support.

Furthermore, the average crystallite size (d_c) of the nanoparticles was calculated with direct use of the Rietveld procedure and the values are included in **Table 3**. The average crystallite size of the bimetallic PtNi nanoparticles supported on BK is larger than that of the particles deposited on TBK and also larger than that of the platinum nanoparticles dispersed over Vulcan XC-72R carbon black.

TABLE 3 | Characteristic parameters of the as-prepared catalysts.

Catalyst	Pt[a]	Ni[a]	Pt[b]	Ni[b]	a_{fcc}	d_c[c]	d_p[d]	*ECSA*[e] $m^2\ g_{Pt}^{-1}$
	at%				nm			
PtNi/BK	69.8	30.2	70.4	29.6	0.3872	4.1	3.6 ± 0.9	61.9
PtNi/TBK	70.3	29.7	71.5	28.5	0.3845	2.9	2.7 ± 0.6	68.8
Pt/C	100	0	100.0	0	0.3916	3.6	3.5 ± 0.7	60.2

[a]*Atomic composition determined by EDX (±3.1 at%).*
[b]*Atomic composition determined by ICP-AES (±1.5 at%).*
[c]*Crystallite size from XRD.*
[d]*Average particle size from HR-TEM.*
[e]*Electrochemical surface area per unit mass determined from CO stripping technique and ICP-AES analysis (±4.1 $m^2\ g^{-1}$).*

Some representative TEM and HR-TEM micrographs, along with the particle size distribution histograms of the bimetallic PtNi nanoparticles supported on BK and TBK biocarbons, are displayed in **Figure 4**. The average particle diameter of all electrocatalysts is compiled in **Table 3** and **Supplementary Table S1**. Overall it can be seen that the biocarbons were covered with well-distributed spherical nanosized particles with diameters ranging from 2.0 to 6 nm. The bimetallic nanoparticles formed over BK have an average diameter of 3.6 nm and the presence of few agglomerates can be observed, while the particles deposited on TBK have an average diameter of 2.7 nm with a narrow particle size distribution. On the other hand, Pt/C catalyst exhibits an average particle size of 3.5 nm, while Pt/BK and Pt/BTK materials have average diameters of 3.4 and 3.0 nm, respectively. The lower average particle diameter and the narrow particle distribution of PtNi/TBK compared to PtNi/BK can be likely explained in terms of the larger specific surface area, the higher roughness, and the higher amount of oxygen- and nitrogen-containing functional groups on the surface of the acid-treated biocarbon. Similar results were reported elsewhere (Antolini, 2009; Hsieh et al., 2013; Sebastián et al., 2013; Zhao et al., 2014; Comignani et al., 2017). On the one hand, the greater the specific BET surface area of the carbon support, the higher the number of surface defects that are present on its surface and the better the particle distribution over the carbonaceous support. And, on the other hand, the higher the number of oxygen and nitrogen functionalities the lower the particle size and the better

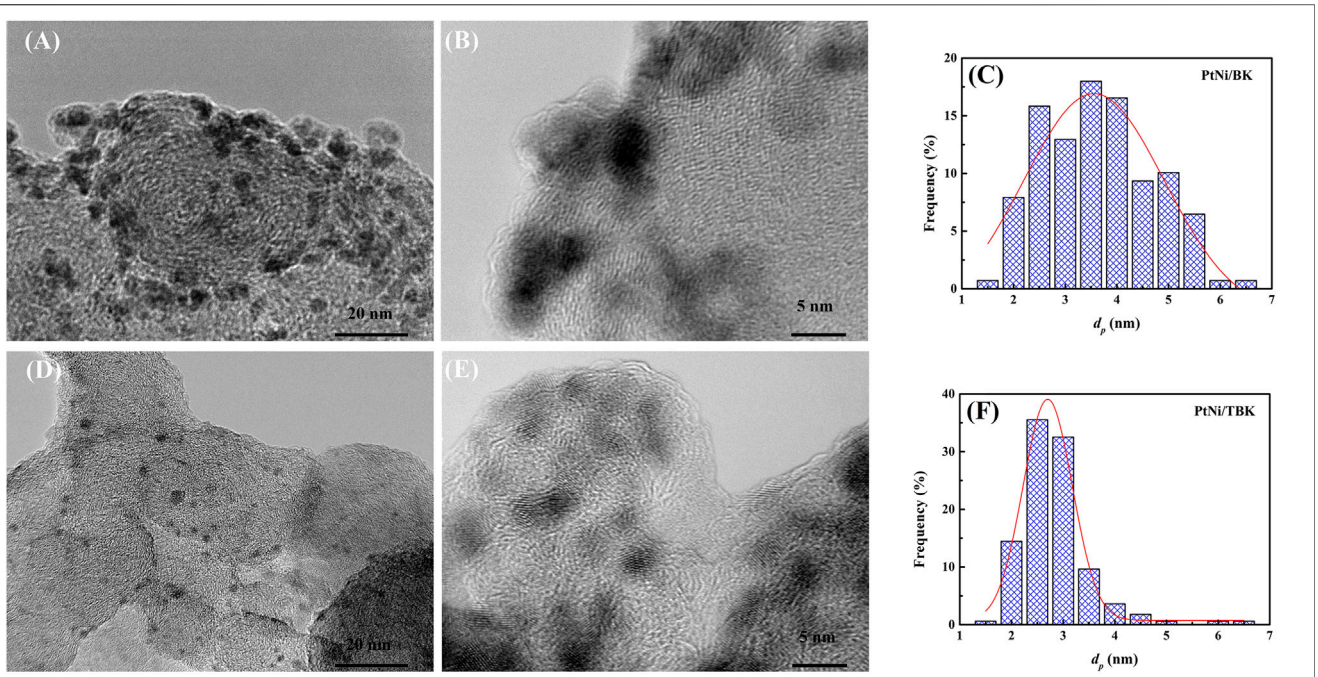

FIGURE 4 | Representative TEM and HR-TEM images and the corresponding particle size distribution histograms of the bimetallic PtNi nanoparticles supported on BK **(A–C)** and TBK **(D–F)** biocarbons.

the particle distribution due to the anchoring effect of surface groups.

Electrochemical Characterization

Figure 5A shows the CO stripping curves obtained at 25°C and a sweep rate of 0.02 V s^{-1}. The voltammetric response of Pt/C electrode was included for comparison. It is found that the onset potential for the electrooxidation of adsorbed CO on PtNi/BK and PtNi/TBK electrodes is shifted negatively by ca. 0.19 V relative to the Pt/C electrode. The oxidation of CO_{ad} on PtNi/BK and PtNi/TBK electrodes begins at 0.150 and 0.140 V respectively, while the onset potential for CO_2 formation on Pt/C is located at 0.34 V. And, the maximum of the CO_{ad} stripping peak on PtNi/BK and PtNi/TBK electrodes is centered at 0.43 and 0.45 V respectively, while it is shifted by ca. 80 mV to a more positive potential on Pt/C (0.53 V). From these results it can be deduced that the oxidative removal of CO on the PtNi nanoparticles supported onto the biocarbons is much easier than that on Pt/C electrode because of Ni atoms provides -OH labile groups through the dissociative adsorption of water at a lower potential that on Pt, and these -OH_{ad} groups facilitate the oxidation of adsorbed carbon monoxide to CO_2 via the so-called bifunctional mechanism (Watanabe and Motoo, 1975; Gasteiger et al., 1993) and because of some surface oxygen functionalities such as hydroxyl and carboxylic acid moieties also provides -OH_{ad} species to promote the oxidation of CO at Pt sites (Antonucci et al., 1994; Hsieh et al., 2013). In addition, the nickel atoms in the bimetallic alloy can modify the d-band properties of Pt atoms at the Fermi level due to the partial electron transfer from the oxophilic metal to Pt (Zhou et al., 2011; Luo et al., 2013; Wang et al. 2014; Zhang et al., 2017). This produces the downshift in the d-band center of Pt (i.e., ligand effect), thus weaken the Pt-CO bond (Goodenough et al., 1989; Nørskov et al., 2009).

The electrochemical surface areas per unit mass of platinum (*ECSA*) calculated from CO stripping of PtNi/KB, PtNi/TBK, Pt/BK, Pt/TBK and Pt/C are summarized in **Table 3** and **Supplementary Table S1**. The highest electrochemical surface area is achieved with the bimetallic nanoparticles supported on the acid-treated biochar, followed Pt/TBK, PtNi/BK, Pt/BK and Pt/C in order of decreasing average *ECSA* values. It can be deduced that the *ECSA* values are directly connected with the particle size, particle size distribution, and particle dispersion onto the different carbonaceous supports. As was commented earlier, this can be ascribed to the available number of anchoring sites for particle deposition, which depends on the BET surface area, the surface roughness and the amount of oxygen and nitrogen functionalities.

The electrooxidation of ethanol in acid environment was studied by cyclic voltammetry at 25 and 60°C and a sweep rate of 0.05 V s^{-1}. The voltammetric curves after fifty cycles are displayed in **Figures 5BC** and **Supplementary Figure S5**. The CV curves recorded at 25°C exhibit the typical features of the electrooxidation of the alcohol on Pt-based electrocatalysts, that is, one anodic peak during the forward scan direction and one anodic peak during the reverse scan direction. The anodic peak in the forward scan is attributed to the oxidation of different chemisorbed species formed through the dehydrogenation of adsorbed ethanol molecules, while the oxidation peak in the reverse scan is ascribed to both the oxidative removal of the

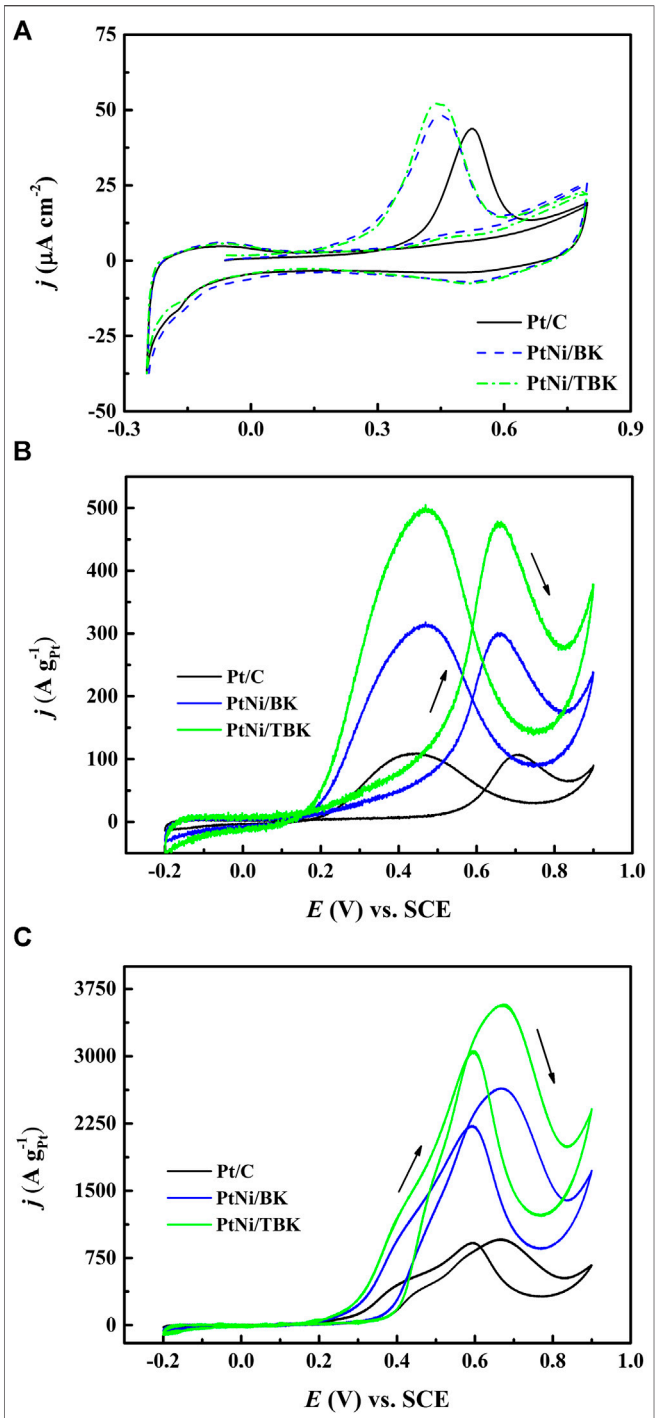

FIGURE 5 | (A) Voltammetric response for adsorbed CO stripping on the Pt/C, PtNi/BK and PtNi/TBK electrocatalysts in 0.1 M H_2SO_4 at 20 mV s^{-1}. Steady cyclic voltammograms (50th cycle) for the different electrodes in 1 M CH_3CH_2OH/0.5 M H_2SO_4 at 25°C **(B)** and 60°C **(C)**.

strongly adsorbed intermediates formed during the forward scan and the oxidation of freshly adsorbed ethanol molecules on free Pt sites. The onset potential for the EOR on PtNi/TBK electrode at 25°C was found to be located at 0.17 V, which is negatively shifted around 0.03 and 0.32 V with respect to the PtNi/BK electrode and Pt/C. The voltammetric curves also showed that the bimetallic PtNi nanoparticles supported on the biocarbon derived from the acid-treated KP displays the highest electroactivity over the whole potential range, followed by PtNi/BK and Pt/C in order of decreasing activity. As shown in **Figure 5B**, the PtNi/TBK electrode developed a maximum mass current density of 476 A g_{Pt}^{-1}, while forward peak current densities of 300 and 107 A g_{Pt}^{-1} were obtained for PtNi/BK and Pt/C electrodes, respectively. That is, the catalytic activity of PtNi/TBK for the EOR process was 1.6 and 7 times higher than that of PtNi/BK and Pt/C, respectively. Moreover, the maximum peak current density on PtNi/TBK catalyst occurred at 0.63 V, which was negatively shifted by ca. 30 and 50 mV with respect to the PtNi/BK and Pt/C electrodes. Therefore, the results point out that the EOR on the PtNi/TBK electrode was easier and faster, and needed less overpotential to occur when compared to the other electrocatalysts. On the other hand, the mass peak current density for Pt/BK was 142 A g_{Pt}^{-1} and for Pt/TBK was 160 A g_{Pt}^{-1}, which were 1.3 and 1.5 times higher than that of Pt/C (**Supplementary Figure S5**). Furthermore, the onset potential for the EOR on Pt/BK and Pt/TBK was negatively shifted as compared to Pt/C by 0.05 and 0.25 V, respectively. Accordingly, it can be demonstrated that the Pt nanoparticles deposited over the biocarbons are capable of catalyzing the ethanol oxidation reaction with greater efficiency than those supported on the commercial carbon black. This result can be explained in terms of the density of surface functional groups and the BET specific surface area of the carbonaceous materials.

Figure 5C shows the stabilized voltammetric response of the as-prepared electrocatalysts for ethanol electrooxidation at 60 °C. It can be observed that with increasing temperature, the onset potentials and the peak potentials shift slightly to less positive values. Besides, the mass specific activities rise up to 3,574, 2,645 and 959 A g_{Pt}^{-1} for PtNi/TBK, PtNi/BK and Pt/C, respectively, as the temperature of the solution increases from 25 to 60°C because of an overall enhancement of the reaction kinetics and a higher electrochemical conversion efficiency of ethanol to CO_2 and other reaction products (Lima et al., 2008; Sun et al., 2009; Altarawneh et al., 2018). Moreover, the shape of the voltammograms is somewhat different from that recorded at 25°C. In the positive scan, the potentiodynamic curves exhibited the main anodic oxidation peak centered at about 0.67, together with a shoulder peak at ca. 0.40 V. In the reverse scan, the oxidative peak occurred at 0.60 V with a shoulder on the left side at ca. 0.5 V. According to the literature, the anodic shoulders can likely be attributed to the formation of CO_2 via both oxidation of CO_{ad} preformed at lower overpotentials and cleavage of C-C bond and subsequent oxidation of the resulting adsorbed C1 species (Wang et al., 2006; Sun et al., 2009). The mass specific current densities of the shoulder peak were determined to be 1,300 A g_{Pt}^{-1} for PtNi/TBK, 1,092 A g_{Pt}^{-1} for PtNi/BK and 416 A g_{Pt}^{-1} for Pt/C. This result can be explained in terms of the thermal activation of the ethanol oxidation process, as was reported elsewhere (Sun et al., 2009). That is, the selectivity towards complete oxidation of ethanol to CO_2 is drastically enhanced with increasing reaction temperature while the

production of acetaldehyde and acetic acid is at the same time significantly reduced.

To obtain more information about the electrocatalytic performance of the bimetallic nanoparticles supported on the softwood kraft pulp-derived carbonaceous materials for the EOR in acid environment, we performed potentiostatic experiments at an applied potential of 0.5 V and temperatures of 25 and 60°C (**Figure 6**). It can be seen that in all *j-t* curves the current density abruptly decreases within the first minutes, due to the formation of different strongly adsorbed intermediates during the EOR. And then, the current densities decrease slowly with time elapsing and reach a pseudo stationary value after 3,000 s because of a relative balance between the oxidative removal of poisoning species at Pt sites via the bifunctional mechanism and the oxidation of freshly ethanol molecules on the regenerated Pt sites. The chronoamperometric curves display that the electrodes follow a similar trend in activity as observed in the potentiodynamic tests, that is, the catalytic activity for ethanol oxidation decreases in the order PtNi/TBK > PtNi/BK > Pt/C. The catalytic activities extracted from the CA curves after 75 min are compiled in **Table 4**. As noted, the bimetallic PtNi nanoparticles supported on TBK can oxidize the ethanol molecules in acid medium more efficiently than the other catalysts, and its catalytic activity at room temperature was improved by factors of 1.3 and 6.3 compared to PtNi/BK and Pt/C, respectively. Moreover, the stable current density at 60°C on PtNi/TBK catalyst was found to be about 1.6 and 7.2 times higher than on PtNi/BK and Pt/C, respectively. In addition, the EDX analysis of the samples before and after the long-term potentiostatic experiments was performed to evaluate the structural stability of the bimetallic nanoparticles (**Supplementary Figure S6; Supplementary Table S2**). By comparing the EDX results reported in **Table 3** with those included in **Supplementary Table S2**, it can be observed that the composition of catalysts remains almost unchanged after the EOR test, thus confirming the good structural stability of the bimetallic nanoparticles supported on the biocarbons.

Both potentiodynamic and potentiostatic experiments clearly show that the overall EOR process turns out to be more favorably on PtNi/TBK and PtNi/BK catalysts than on Pt/C. These results are in accordance with those extracted from the CO-stripping experiments. The better performance of the bimetallic catalysts can be partially explained by the ability of surface Ni and Ni related species to form labile -OH_{ad} at more negative potentials than Pt, and the partial electron transfer from Ni to Pt that generates the downshift in the d-band center of Pt, which markedly alters the metal electronic structures thus weakening the adsorption of CO and other poisoning reaction intermediates like acetaldehyde (Almeida et al., 2011; Antolini et al., 2005; Comignani et al., 2015). Besides, the compressive strain induced by incorporation of Ni result in lattice mismatch and d-band center downshifts of Pt, thereby also weakening the binding strength of CO and other intermediates on the surface of the catalysts (Nørskov, et al., 2009; Li et al., 2012). Apart from the favorable effect of Ni, the presence of labile hydroxyl species on the surface of the biocarbons could also contribute to the enhanced performance of the bimetallic nanoparticles (Antonucci et al., 1994).

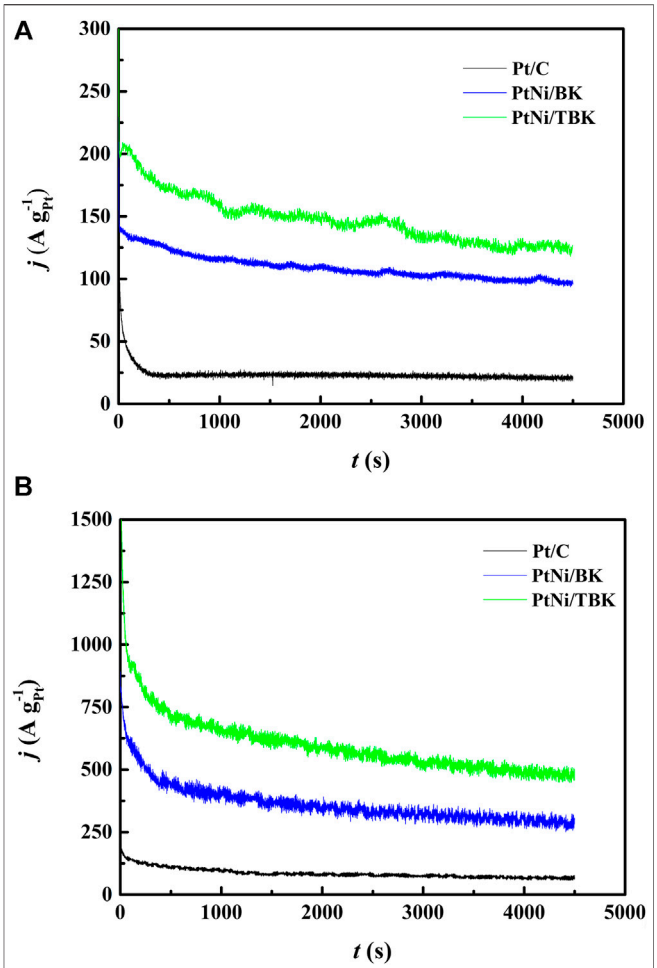

FIGURE 6 | Current-time curves at 0.5 V vs. *SCE* for Pt/C, PtNi/BK and PtNi/TBK electrodes in a 1 M CH_3CH_2OH + 0.5 M H_2SO_4 solution at 25°C **(A)** and 60°C **(B)**.

TABLE 4 | Specific mass activities of PtNi/TBK, PtNi/BK and Pt/C electrodes for ethanol oxidation in 1 M EtOH/0.5 M H_2SO_4 solution at an applied potential of 0.5 V vs. *SCE*.

	25°C	60°C
Catalyst	*j* A g_{Pt}^{-1}	
PtNi/BK	96	294
PtNi/TBK	125	480
Pt/C	20	67

In order to rationalize the better electrocatalytic performance of the PtNi/TKB catalyst compared to PtNi/BK electrode, it is important to consider the influence of the textural and surface properties of the biocarbons on the alloying degree of Ni with Pt, the chemical state of Ni, particle size and dispersion. But let us first turn our attention to discuss the direct influence of the biocarbons in the electrocatalytic oxidation of ethanol in the acid electrolyte. The surface oxygen and nitrogen functionalities, such

as carboxylic, hydroxyl and pyrrolic moieties, are capable of providing labile -OH species to facilitate the oxidation of adsorbed intermediates via the bifunctional mechanism (Zhou et al., 2010; Calderón et al., 2012; Hsieh et al., 2012; Zhang et al., 2014). Therefore, taking into account that the density of surface functional groups on TBK biocarbon is higher than that on the biocarbon synthesized with the raw kraft pulp material, more hydroxyl species can be supplied by TBK to oxidize the adsorbed poisoning intermediates and free the electroactive platinum sites for further ethanol oxidation, thus enhancing the overall EOR process. Similar results to those presented here were reported in the literature. For instance, Hsieh et al. found that the presence of surface oxygen functionalities on the surface of carbon nanotubes enhance the anti-poisoning ability of Pt nanoparticles for the electrooxidation of formic acid (Hsieh, et al. 2013). Calderon and coworkers established that the electrocatalytic response of bimetallic PtRu nanoparticles supported on carbon xerogels towards the electrooxidation of methanol is improved by the presence of oxygen functionalities, particularly the carboxylic groups (Calderón et al., 2012). Also, Asgardi et al. suggested that the presence of a larger number of surface oxygenated moieties on carbon support is a determining parameter for enhancing the activity of Pt-based nanoparticles for the EOR process (Asgardi et al., 2015). On the other hand, the electrical conductivity is expected to have a negligible influence on the EOR process because both biomass-derived carbonaceous materials presented similar conductivity values. Let us now shift the analysis from the direct correlation between the carbon support properties and the catalytic activity to the influence of the support properties on the bimetallic nanoparticles (i.e., an indirect relation between support properties and catalytic activity). The BET specific surface area and the density of surface functional groups have a positive effect on particle size and distribution, and thus in *ECSA*. Therefore, the resulting mass activity increased with increasing the electroactive surface area. So, the difference in the *ECSA* of catalysts can explain in part the better performance of PtNi/TBK catalyst with respect to PtNi/BK. In a previous report, we demonstrated that the functionalization of carbon supports via acid treatment caused a reduction in the particle size and induced better dispersion of nanoparticles, which in turn results in increased catalytic activity towards methanol and ethanol oxidation reactions (Comignani et al., 2017). Similar conclusions were reached for several investigations concerning the influence of textural properties and surface chemistry of carbon supports on the electrocatalytic properties of nanosized catalysts (Celorrio et al., 2012; Sebastián et al., 2012; Hsieh et al., 2013; Sebastián et al., 2014). For instance, Cellorrio et al. found that Pd nanoparticles supported on a highly oxidized Vulcan support exhibit better electrocatalytic activity for the oxidation of formic acid than the nanoparticles supported on the pristine carbon powder (Celorrio et al., 2012). Sebastián and collaborators found that the *ECSA* and ORR activity of carbon supported Pt nanoparticles depends on the density of surface oxygen functionalities and ghaphicity (Sebastián et al., 2012). With regards to alloying degree and the chemical state of Ni, it is noted that the different physicochemical surface properties of the biocarbons led to the formation of nanoparticles with different nickel content in the alloy. The causes for the different Ni content in the bimetallic alloy are not clear yet, and this will be the object of future studies. Although, it is hypothesized that the difference in the alloyed and non-alloyed Ni content could be associated with a more effective reduction of nickel ions on TBK than on BK due to its higher amount of surface functionalities and surface defects. Antolini indicated that the high activity of PtNi catalysts for the methanol oxidation is a consequence of the synergic effect between alloyed and non-alloyed nickel atoms, where alloyed Ni facilitates the dehydrogenation of the molecules and non-alloyed Ni makes easier the removal of adsorbed CO (Antolini, 2017). As indicated above, the observed difference in activity can to some extent be explained by a compromise between the number of alloyed and non-alloyed nickel atoms. The alloyed nickel atoms can accomplish a dual role. On the one hand, they can promote the dehydrogenation steps of the EOR and, on the other hand, they can modify the electronic structure of Pt atoms at the Fermi level, which weakens the bonding energy between Pt and CO-like intermediates. Whereas, the non-alloyed nickel atoms works as an $-OH_{ad}$ supplier that accelerates the oxidation of the poisoning intermediates via the bifunctional mechanism. Some authors studied the effect of Ni content on the electrocatalytic activity of PtNi catalysts, and found that the methanol oxidation reaction is favored by the presence of both alloyed and non-alloyed nickel

TABLE 5 | Performance of different electrocatalysts for the EOR process in acid medium.

Catalyst	Support	Electrolyte and fuel	E_{onset}[a], V	j_p[b], A g_{Pt}^{-1}	j[a,c], A g_{Pt}^{-1}	Reference
Pt nanowires	Porous carbon spheres from pectin	0.5 M H_2SO_4, 1 M EtOH	0.5 V	278 (RT[d])	30.0 (0.65 V)	Fan et al., 2015
PtSn/a-BC	Biocarbon from *Eucaliptus grandis* wood	0.5 M H_2SO_4, 1 M EtOH	0.19	71.1 (25 °C)	-	da Silva et al., 2014
$Pt_{2.3}Ni$/C octahedra	Carbon black	0.1 M $HClO_4$, 0.2 M EtOH	0.21	638 (RT)	65.9 (0.40 V)	Sulaiman et al., 2017
$PtSnO_2$/CNT	MWCNTs	1 M $HClO_4$, 1 M EtOH	0.46	554 (RT)	40.0 (0.4 V)	Song et al., 2016
PtSnRu nanorods	GC	0.5 M H_2SO_4, 1 M EtOH	0.45	437.9 (RT)	27.9 (0.4 V)	Huang et al., 2019
PtSnCe/C	Carbon black	0.5 M H_2SO_4, 0.5 M EtOH	0.25	380 (25 °C)	143.2 (0.36 V)	Jacob et al., 2015
Pt-Mo-Ni nanowires	GC	0.5 M H_2SO_4, 2 M EtOH	0.10	865.8 (RT)	109 (0.5 V)	Mao et al., 2017
$Pt_{0.7}Ni_{0.3}$	Biocarbon from acid-treated kraft pulp (TBK)	0.5 M H_2SO_4, 1 M EtOH	0.17	476 (25 °C)	125 (0.5 V)	This work

[a]*The electrode potentials were referred to the SCE scale.*
[b]*Sweep rate of 50 mV* s^{-1}.
[c]*Current density extracted from CA experiments.*
[d]*Room Temperature.*

atoms (Luo et al., 2013; Nassr et al., 2013; Wang et al., 2014). Probably, the higher efficiency of PtNi/TBK can be either explained in terms of the better tolerance to poisoning of alloyed than non-alloyed PtNi nanoparticles (Antolini, 2017) or a better compromise between the structural effects produced by alloyed nickel atoms (*i.e.*, electronic and compressive strain effects) and oxophilicity effect generated by non-alloyed nickel atoms (*i.e.*, bifunctional mechanism).

Finally, the as-prepared PtNi nanoparticles supported on the biocarbons synthesized from the treated fibrous fraction of unbleached softwood kraft-liner paper exhibited very competitive activities for the EOR when compared to recent results published in the literature (**Table 5**). For instance, da Silva et al. prepared activated biocarbon from *Eucalyptus grandis* wood (S_{BET} = 787 $m^2 g^{-1}$, V_T = 0.47 $cm^3 g^{-1}$ and O content = 9.86 at. %) as Pt and PtSn catalyst support for the EOR process and obtained peak current densities of 16.5 and 71.1 A g_{Pt}^{-1}, respectively (da Silva et al., 2014). Fang and coworkers synthesized pectin-derived porous carbon spheres (S_{BET} = 2,440 $m^2 g^{-1}$ and V_T = 1.28 $cm^3 g^{-1}$) as Pt catalyst support (Fan et al., 2015). The as-prepared electrocatalysts developed a peak current density of 278 A g_{Pt}^{-1} and an activity of ca. 30 A g_{Pt}^{-1} at 0.65 V vs. *SCE* for the EOR in acid environment.

Further research will be focused on evaluating the influence of the pretreatment and pyrolysis temperature on the textural and structural properties of the biocarbons obtained from softwood kraft pulp. The as-synthesized biocarbons will be employed as supports of Pt-based nanoparticles with low noble metal content and core-shell structure for ethanol and glycerol electrooxidations.

CONCLUSIONS

The pristine and phosphoric acid-treated fibers of unbleached softwood kraft pulp were used to fabricate biocarbons via fast pyrolysis. The biocarbon derived from the kraft pulp (BK) has a BET surface area of 306 $m^2 g^{-1}$ and a total pore volume 1.2 $cm^3 g^{-1}$, whereas the biocarbon derived from the acid-treated has a specific surface area of 454 $m^2 g^{-1}$ and a total pore volume of 1.8 $cm^3 g^{-1}$. Besides, the biocarbons also show different oxygen and nitrogen contents. The as-synthesized biocarbons were employed as supports of PtNi nanoparticles formed by pulse microwave-assisted reduction in ethylene glycol. PtNi particles with average diameters in the range of 2.9–4.1 nm and a nickel content of ca. 30 at% are obtained. It was determined that ca. 37% of Ni atoms are forming an alloy with Pt in the PtNi/BK catalyst, while ca. 61% of Ni atoms are forming an alloy in the PtNi/TBK catalyst.

The electrocatalytic properties of the as-synthesized electrocatalysts for the EOR in acid medium were tested by means of cyclic voltammetry and chronoamperometry at temperatures of 25 and 60°C. The experiments show that the PtNi/TBK material can catalyze the electrooxidation of ethanol more efficiently than the other catalysts, and its mass activity was improved by factors around 1.5 and 7 with respect to PtNi/BK and Pt/C, respectively. The better performance of the PtNi/TKB electrode was explained through the combination of several factors: 1) the higher density of surface functional groups on the surface of TBK, 2) the small average particle size and narrow particle distribution (i.e., higher ECSA value), and 3) the better compromise between the number of alloyed and non-alloyed nickel atoms.

DATA AVAILABILITY STATEMENT

The original contributions presented in the study are included in the article/**Supplementary Material**, further inquiries can be directed to the corresponding author/s.

AUTHOR CONTRIBUTIONS

MNL conducted the experiments, analyzed data and performed writing. JS conceived the idea, conducted the experiments, analyzed data and performed writing, review and editing. EM conceived the idea and performed writing.

FUNDING

This investigation was supported by ANPCyT, Universidad Nacional del Sur and Universidad Nacional de Córdoba through grants PICT2014 No. 3393, PGI 24/M167 and SECyT 313/16.

ACKNOWLEDGMENTS

MNL thanks CONICET for a postdoctoral fellowship.

SUPPLEMENTARY MATERIAL

The Supplementary Material for this article can be found online at: https://www.frontiersin.org/articles/10.3389/fmats.2020.588399/full#supplementary-material

REFERENCES

Almeida, T. S., Kokoh, K. B., Kokoh, K. B., and De Andrade, A. R. (2011). Effect of Ni on Pt/C and PtSn/C prepared by the Pechini method. *Int. J. Hydrogen Energy.* 36, 3803–3810. doi:10.1016/j.ijhydene.2010.12.066.

Altarawneh, R. M., Brueckner, T. M., Chen, B., and Pickup, P. G. (2018). Product distributions and efficiencies for ethanol oxidation at PtNi octahedra. *J. Power Sources.* 400, 369–376. doi:10.1016/j.jpowsour.2018.08.052.

Antolini, E. (2009). Carbon supports for low-temperature fuel cell catalysts. *Appl. Catal. B Environ.* 88, 1–24. doi:10.1016/j.apcatb.2008.09.030.

Antolini, E. (2017). Pt-Ni and Pt-M-Ni (M = Ru, Sn) anode catalysts for low-temperature acidic direct alcohol fuel cells: a review. *Energies.* 10, 42. doi:10.3390/en10010042.

Antolini, E., Salgado, J. R. C., and González, E. R. (2005). Carbon supported Pt75M25 (M=Co, Ni) alloys as anode and cathode electrocatalysts for direct

methanol fuel cells. *J. Electroanal. Chem.* 580, 145–154. doi:10.1016/j.jelechem.2005.03.023.

Antonucci, P. L., Alderucci, V., Giordano, N., Cocke, D. L., and Kim, H. (1994). On the role of surface functional groups in Pt carbon interaction. *J. Appl. Electrochem.* 24, 58–65. doi:10.1007/bf00243330.

Asgardi, J., Calderón, J. C., Alcaide, F., Querejeta, A., Calvillo, L., Lázaro, M. J., et al. (2015). Carbon monoxide and ethanol oxidation on PtSn supported catalysts: effect of the nature of the carbon support and Pt:Sn composition. *Appl. Catal. B Environ.* 168–169, 33–41. doi:10.1016/j.apcatb.2014.12.003.

Bengtsson, A., Hecht, P., Sommertune, J., Ek, M., Sedin, M., and Sjöholm, E. (2020). Carbon fibers from lignin-cellulose precursors: effect of carbonization conditions. *ACS Sustain. Chem. Eng.* 8, 6826–6833. doi:10.1021/acssuschemeng.0c01734.

Beyhan, S., Léger, J.-M., and Kadırgan, F. (2013). Pronounced synergetic effect of the nano-sized PtSnNi/C catalyst for ethanol oxidation in direct ethanol fuel cell. *Appl. Catal. B Environ.* 130–131, 305- 313. doi:10.1016/j.apcatb.2012.11.007.

Calderón, J. C., Mahata, N., Pereira, M. F. R., Figueiredo, J. L., Fernandes, V. R., Rangel, C. M., et al. (2012). Pt-Ru catalysts supported on carbon xerogels for PEM fuel cells. *Int. J. Hydrogen Energy.* 37, 7200–7211. doi:10.1016/j.ijhydene.2011.12.029.

Celorrio, V., Montes de Oca, M. G., Plana, D., Moliner, R., Fermín, D. J., and Lázaro, M. J. (2012). Electrochemical performance of Pd and Au-Pd core-shell nanoparticles on surface tailored carbon black as catalyst support. *Int. J. Hydrogen Energy.* 37, 7152–7160. doi:10.1016/j.ijhydene.2011.12.014.

Comignani, V., Sieben, J. M., Brigante, M. E., and Duarte, M. M. E. (2015). Carbon supported Pt-NiO nanoparticles for ethanol electro-oxidation in acid media. *J. Power Sources.* 278, 119–127. doi:10.1016/j.jpowsour.2014.12.063.

Comignani, V., Sieben, J. M., Sanchez, M. D., and Duarte, M. M. E. (2017). Influence of carbon support properties on the electrocatalytic activity of PtRuCu nanoparticles for methanol and ethanol oxidation. *Int. J. Hydrogen Energy.* 42, 24785–24796. doi:10.1016/j.ijhydene.2017.08.079.

da Silva, E. L., Ortega Vega, M. R., Correa, P. d. S., Cuña, A., Tancredi, N., and Malfatti, C. d. F. (2014). Influence of activated carbon porous texture on catalyst activity for ethanol electro-oxidation, *Int. J. Hydrogen Energy.* 39, 14760–14767. doi:10.1016/j.ijhydene.2014.07.103.

Dobele, G., Meier, D., Faix, O., Radtke, S., Rossinskaja, G., and Telysheva, G. (2001). Volatile products of catalytic flash pyrolysis of celluloses. *J. Anal. Appl. Pyrol.* 58–59, 453–463. doi:10.1016/S0165-2370(00)00128-5.

El Qada, E. N., Allen, S. J., and Walker, G. M. (2008). Influence of preparation conditions on the characteristics of activated carbons produced in laboratory and pilot scale systems. *Chem. Eng. J.* 142, 1–13. doi:10.1016/j.cej.2007.11.008.

Falco, C., Sieben, J. M., Brun, N., Sevilla, M., van der Mauelen, T., Morallón, E., et al. (2013). Hydrothermal carbons from hemicellulose-derived aqueous hydrolysis products as electrode materials for supercapacitors. *ChemSusChem.* 6, 374–382. doi:10.1002/cssc.201200817.

Fan, Y., Liu, P.-F., Yang, Z.-J., Jiang, T.-W., Yao, K.-L., Han, R., et al. (2015). Bi-functional porous carbon spheres derived from pectin as electrode material for supercapacitors and support material for Pt nanowires towards electrocatalytic methanol and ethanol oxidation. *Electrochim. Acta.* 163, 140–148. doi:10.1016/j.electacta.2015.02.157.

Gasteiger, H. A., Markovic, N., Ross, P. N., and Cairns, E. J. (1993). Methanol electrooxidation on well-characterized platinum-ruthenium bulk alloys. *J. Phys. Chem.* 97, 12020–12029. doi:10.1021/j100148a030.

Gong, X., Liu, S., Ouyang, C., Strasser, P., and Yang, R. (2015). Nitrogen- and phosphorus-doped biocarbon with enhanced electrocatalytic activity for oxygen reduction. *ACS Catal.* 5, 920–927. doi:10.1021/cs501632y.

González-García, P., Centeno, T. A., Urones-Garrote, E., Ávila-Brande, D., and Otero-Díaz, L. C. (2013). Microstructure and surface properties of lignocellulosic-based activated carbons. *Appl. Surf. Sci.* 265, 731–737. doi:10.1016/j.apsusc.2012.11.092.

Goodenough, J. B., Manoharan, R., Shukla, A. K., and Ramesh, K. V. (1989). Intraalloy electron transfer and catalyst performance: a spectroscopic and electrochemical study. *Chem. Mater.* 1, 391–398. doi:10.1021/cm00004a003.

Guo, C.-Z., Liao, W.-L., and Chen, C.-G. (2014). Design of a non-precious metal electrocatalyst for alkaline electrolyte oxygen reduction by using soybean biomass as the nitrogen source of electrocatalytically active center structures. *J. Power Sources.* 269, 841–847. doi:10.1016/j.jpowsour.2014.07.024.

Habibi, B., and Dadashpour, E. (2013). Carbon-ceramic supported bimetallic Pt-Ni nanoparticles as an electrocatalyst for electrooxidation of methanol and ethanol in acidic media. *Int. J. Hydrogen Energy.* 38, 5425–5434. doi:10.1016/j.ijhydene.2012.06.045.

Haq, I., and Raj, A. (2020). "Pulp and paper mill wastewater: ecotoxicological effects and bioremediation approaches for environmental safety," in *Bioremediation of industrial waste for environmental safety: volume II: biological agents and methods for industrial waste management.*. R. N. Bharagava and G. Saxena (Editors) (Singapore: Springer), 333–356.

Hsieh, C.-T., Chen, W.-Y., Tzou, D.-Y., Roy, A. K., and Hsiao, H.-T. (2012). Atomic layer deposition of Pt nanocatalysts on graphene oxide nanosheets for electro-oxidation of formic acid. *Int. J. Hydrogen Energy.* 37, 17837–17843. doi:10.1016/j.ijhydene.2012.08.139.

Hsieh, C.-T., Gu, J.-L., Tzou, D.-Y., Chu, Y.-C., and Chen, Y.-C. (2013). Microwave deposition of Pt catalysts on carbon nanotubes with different oxidation levels for formic acid oxidation. *Int. J. Hydrogen Energy.* 38, 10345–10353. doi:10.1016/j.ijhydene.2013.05.146.

Huang, T.-H., Zheng, H.-S., Cheng, Y.-M., Liu, C.-W., Lee, S.-W., Wang, J.-H., et al. (2019). The preparation and mechanistic study of highly effective PtSnRu ternary nanorod catalysts toward the ethanol oxidation reaction. *Sustain. Energy Fuels.* 3, 3352–3362. doi:10.1039/c9se00474b.

Imanzadeh, H., and Habibi, B. (2020). Electrodeposition of ternary CuNiPt alloy nanoparticles on graphenized pencil lead electrode as a new electrocatalyst for electro-oxidation of ethanol. *Solid State Sci.* 105, 106239. doi:10.1016/j.solidstatesciences.2020.106239.

Jacob, J. M., Corradini, P. G., Antolini, E., Abe Santos, N., Santos, N. A., and Perez, J. (2015). Electro-oxidation of ethanol on ternary Pt-Sn-Ce/C catalysts. *Appl. Catal. B Environ.* 165, 176–184. doi:10.1016/j.apcatb.2014.10.012.

Kacuráková, M., Capek, P., Sasinková, V., Wellner, N., and Ebringerová, A. (2000). FT-IR study of plant cell wall model compounds: pectic polysaccharides and hemicelluloses. *Carbohydr. Polym.* 43, 195–203. doi:10.1016/S0144-8617(00)00151-X.

Kennedy, L. J., Vijaya, J. J., and Sekaran, G. (2004). Effect of two-stage process on the preparation and characterization of porous carbon composite from rice husk by phosphoric acid activation. *Ind. Eng. Chem. Res.* 43, 1832–1838. doi:10.1021/ie034093f.

Klemm, D., Heublein, B., Fink, H., and Bohn, A. (2005). Cellulose: Fascinating biopolymer and sustainable raw material Angewandte. *Polym. Sci.* 44, 3358–3393. doi:10.1002/anie.200460587.

Li, M., Liu, P., and Adzic, R. R. (2012). Platinum monolayer electrocatalysts for anodic oxidation of alcohols. *J. Phys. Chem. Lett.* 3, 3480–3485. doi:10.1021/jz3016155.

Lima, F. H. B., Profeti, D., Lizcano-Valbuena, W. H., Ticianelli, E. A., and Gonzalez, E. R. (2008). Carbon-dispersed Pt-Rh nanoparticles for ethanol electro-oxidation. Effect of the crystallite size and of temperature. *J. Electroanal. Chem.* 617, 121–129. doi:10.1016/j.jelechem.2008.01.024.

Liu, W.-J., Jiang, H., and Yu, H.-Q. (2019). Emerging applications of biochar-based materials for energy storage and conversion. *Energy Environ. Sci.* 12, 1751–1779. doi:10.1039/C9EE00206E.

Luo, B., Xu, S., Yan, X., and Xue, Q. (2013). PtNi alloy nanoparticles supported on polyelectrolyte functionalized graphene as effective electrocatalysts for methanol oxidation. *J. Electrochem. Soc.* 160, F262–F268. doi:10.1149/2.056303jes.

Mao, J., Chen, W., He, D., Wan, J., Pei, J., Dong, J., et al. (2017). Design of ultrathin Pt-Mo-Ni nanowire catalysts for ethanol electrooxidation. *Sci. Adv.* 3, e1603068. doi:10.1126/sciadv.1603068.

Marinho, B., Ghislandi, M., Tkalya, E., Koning, C. E., and de With, G. (2012). Electrical conductivity of compacts of graphene, multi-wall carbon nanotubes, carbon black, and graphite powder. *Powder Technol.* 221, 351–358. doi:10.1016/j.powtec.2012.01.024.

Nørskov, J. K., Bligaard, T., Rossmeisl, J., and Christensen, C. H. (2009). Towards the computational design of solid catalysts. *Nat. Chem.* 1, 37–46. doi:10.1038/nchem.121.

Nassr, A. B. A. A., Sinev, I., Grünert, W., and Bron, M. (2013). PtNi supported on oxygen functionalized carbon nanotubes: in depth structural characterization and activity for methanol electrooxidation. *Appl. Catal. B Environ.* 142–143, 849–860. doi:10.1016/j.apcatb.2013.06.013.

Nieva Lobos, M. L., Campitelli, P., Volpe, M. A., and Moyano, E. L. (2016a). Catalytic and non-catalytic pyrolysis of Kraft pulp waste into anhydrosugars containing bio-oils and non-phytotoxic biochars. *J. Anal. Appl. Pyrol.* 122, 216–223. doi:10.1016/j.jaap.2016.09.021.

Nieva Lobos, M. L., Sieben, J. M., Comignani, V., Duarte, M., Volpe, M. A., and Moyano, E. L. (2016b). Biochar from pyrolysis of cellulose: an alternative catalyst support for the electro-oxidation of methanol. *Int. J. Hydrogen Energy.* 41, 10695–10706. doi:10.1016/j.ijhydene.2016.04.041.

Pistone, A., and Espro, C. (2020). Current trends on turning biomass wastes into carbon materials for electrochemical sensing and rechargeable battery applications. *Curr. Opin. Green Sustain. Chem.* 26, 100374. doi:10.1016/j.cogsc.2020.100374.

Reckamp, J. M., Garrido, R. A., and Satrio, J. A. (2014). Selective pyrolysis of paper mill sludge by using pretreatment processes to enhance the quality of bio-oil and biochar products. *Biomass Bioenergy.*. 71, 235–244. doi:10.1016/j.biombioe.2014.10.003.

Schonvogel, D., Nowotny, M., Woriescheck, T., Multhaupt, H., Wagner, P., Dyck, A., et al. (2019). Hydrothermal carbonization-derived carbon from waste biomass as renewable Pt support for fuel cell applications: role of carbon activation. *Energy Technol.* 7, 1900344. doi:10.1002/ente.201900344.

Sebastián, D., Lázaro, M. J., Moliner, R., Suelves, I., Aricò, A. S., and Baglio, V. (2014). Oxidized carbon nanofibers supporting PtRu nanoparticles for direct methanol fuel cells. *Int. J. Hydrogen Energy.* 39, 5414–5423. doi:10.1016/j.ijhydene.2013.12.005.

Sebastián, D., Ruíz, A. G., Suelves, I., Moliner, R., Lázaro, M. J., Baglio, V., et al. (2012). Enhanced oxygen reduction activity and durability of Pt catalysts supported on carbon nanofibers. *Appl. Catal. B Environ.* 115–116, 269–275. doi:10.1016/j.apcatb.2011.12.041.

Sebastián, D., Suelves, I., Pastor, E., Moliner, R., and Lázaro, M. J. (2013). The effect of carbon nanofiber properties as support for PtRu nanoparticles on the electrooxidation of alcohols. *Appl. Catal. B Environ.* 132–133, 13–21. doi:10.1016/j.apcatb.2012.11.018.

Shen, Y., Xiao, K., Xi, J., and Qiu, X. (2015). Comparison study of few-layered graphene supported platinum and platinum alloys for methanol and ethanol electro-oxidation. *J. Power Sources.* 278, 235–244. doi:10.1016/j.jpowsour.2014.12.062.

Song, H., Luo, M., Qiu, X., and Cao, G. (2016). Insights into the endurance promotion of PtSn/CNT catalysts by thermal annealing for ethanol electro-oxidation. *Electrochim. Acta.* 213, 578–586. doi:10.1016/j.electacta.2016.07.053.

Suleiman, J. E., Zhu, S., Xing, Z., Chang, Q., and Shao, M. (2017). Pt-Ni octahedra as electrocatalysts for ethanol electro-oxidation reaction. *ACS Catal.* 7, 5134–5141. doi:10.1021/acscatal.7b01435

Sun, F., Wang, L., Peng, Y., Gao, J., Pi, X., Qu, Z., et al. (2018). Converting biomass waste into microporous carbon with simultaneously high surface area and carbon purity as advanced electrochemical energy storage materials. *Appl. Surf. Sci.* 436, 486–494. doi:10.1016/j.apsusc.2017.12.067.

Sun, S., Halseid, M. C., Heinen, M., Jusys, Z., and Behm, R. J. (2009). Ethanol electrooxidation on a carbon-supported Pt catalyst at elevated temperature and pressure: a high-temperature/high-pressure DEMS study. *J. Power Sources.* 190, 2–13. doi:10.1016/j.jpowsour.2009.01.073.

Tzong-Horng, L. (2010). Development of mesoporous structure and high adsorption capacity of biomass-based activated carbon by phosphoric acid and zinc chloride activation. *Chem. Eng. J.* 158, 129–142. doi:10.1016/j.cej.2007.11.008

Van Soest, P. J., Robertson, J. B., and Lewis, B. A. (1991). Methods for dietary fiber, neutral detergent fiber, and nonstarch polysaccharides in relation to animal nutrition. *J. Dairy Sci.* 74, 3583–3597. doi:10.3168/jds.S0022-0302(91)78551-2.

Wang, H., Jusys, Z., and Behm, R. J. (2006). Ethanol electro-oxidation on carbon-supported Pt, PtRu and Pt3Sn catalysts: a quantitative DEMS study. *J. Power Sources.* 154, 351–359. doi:10.1016/j.jpowsour.2005.10.034.

Wang, L.-L., Zhang, D.-F., and Guo, L. (2014). Phase-segregated Pt-Ni chain-like nanohybrids with high electrocatalytic activity towards methanol oxidation reaction. *Nanoscale.* 6, 4635–4641. doi:10.1039/c4nr00139g.

Watanabe, M., and Motoo, S. (1975). Electrocatalysis by ad-atoms. *J. Electroanal. Chem. Interfacial Electrochem.* 60, 267–273. doi:10.1016/s0022-0728(75)80261-0.

Zhang, H., Zeng, Y., Cao, L., Yang, L., Fang, D., Yi, B., et al. (2017). Enhanced electrocatalytic performance of ultrathin PtNi alloy nanowires for oxygen reduction reaction. *Front. Energy.* 11, 260–267. doi:10.1007/s11708-017-0499-x.

Zhang, J., Zhang, J., Lin, L., Chen, T., Zhang, J., Liu, S., et al. (2009). Dissolution of microcrystalline cellulose in phosphoric acid-molecular changes and kinetics. *Molecules.* 14, 5027–5041. doi:10.3390/molecules14125027.

Zhang, Y., Zhu, R., Cui, Y., Zhong, J., Zhang, X., and Chen, J. (2014). PtRu nanoparticles supported on nitrogen-doped polyhedral mesoporous carbons as electrocatalyst for methanol oxidation. *Nanotechnology.* 25, 135607. doi:10.1088/0957-4484/25/13/135607.

Zhao, H., Kwak, J., Conradzhang, Z., Brown, H., Arey, B., and Holladay, J. 2007). Studying cellulose fiber structure by SEM, XRD, NMR and acid hydrolysis. *Carbohydr. Polym.* 68, 235–241. doi:10.1016/j.carbpol.2006.12.013.

Zhao, X., Zhu, J., Liang, L., Li, C., Liu, C., Liao, J., et al. (2014). Biomass-derived N-doped carbon and its application in electrocatalysis. *Appl. Catal. B Environ.* 154–155, 177–182. doi:10.1016/j.apcatb.2014.02.027.

Zhou, X.-W., Zhang, R.-H., Zhou, Z.-Y., and Sun, S.-G. (2011). Preparation of PtNi hollow nanospheres for the electrocatalytic oxidation of methanol. *J. Power Sources.* 196, 5844–5848. doi:10.1016/j.jpowsour.2011.02.088.

Zhou, Y., Neyerlin, K., Olson, T. S., Pylypenko, S., Bult, J., Dinh, H. N., et al. (2010). Enhancement of Pt and Pt-alloy fuel cell catalyst activity and durability via nitrogen-modified carbon supports. *Energy Environ. Sci.* 3, 1437–1446. doi:10.1039/C003710A.

Conflict of Interest: The authors declare that the research was conducted in the absence of any commercial or financial relationships that could be construed as a potential conflict of interest.